

Structure-Aware Near-Field Radio Map Recovery via RBF-Assisted Matrix Completion

Hao Sun, Xianghao Yu, *Senior Member, IEEE*, and Junting Chen, *Member, IEEE*

Abstract—This paper proposes a novel structure-aware matrix completion framework assisted by radial basis function (RBF) interpolation for near-field radio map construction in extremely large multiple-input multiple-output (XL-MIMO) systems. Unlike the far-field scenario, near-field wavefronts exhibit strong dependencies on both angle and distance due to spherical wave propagation, leading to complicated variations in received signal strength (RSS). To effectively capture the intricate spatial variations structure inherent in near-field environments, a regularized RBF interpolation method is developed to enhance radio map reconstruction accuracy. Leveraging theoretical insights from interpolation error analysis of RBF, an inverse μ -law-inspired non-uniform sampling strategy is introduced to allocate measurements adaptively, emphasizing regions with rapid RSS variations near the transmitter. To further exploit the global low-rank structure in the near-field radio map, we integrate RBF interpolation with nuclear norm minimization (NNM)-based matrix completion. A robust Huberized leave-one-out cross-validation (LOOCV) scheme is then proposed for adaptive selection of the tolerance parameter, facilitating optimal fusion between RBF interpolation and matrix completion. The integration of local variation structure modeling via RBF interpolation and global low-rank structure exploitation via matrix completion yields a structure-aware framework that substantially improves the accuracy of near-field radio map reconstruction. Extensive simulations demonstrate that the proposed approach achieves over 10% improvement in normalized mean squared error (NMSE) compared to standard interpolation and matrix completion methods under varying sampling densities and shadowing conditions.

Index Terms—Huberized leave-one-out cross-validation, matrix completion, near-field radio map, non-uniform sampling, radial basis function, structure-aware.

I. INTRODUCTION

Sixth-generation (6G) wireless communication is envisioned to provide ultra-high data rates, massive device connectivity, and high precision localization and sensing [1]–[3]. A key enabler of these capabilities is the deployment of extremely large multiple-input multiple-output (XL-MIMO) systems, which increases the number of antennas by an order of magnitude and expands the array aperture to the meter scale. This substantial aperture expansion fundamentally alters the electromagnetic propagation regime by enlarging the radiative near-field region, where wavefront curvature becomes non-negligible. The boundary of this region, characterized

by the Rayleigh distance, scales quadratically with aperture size, bringing near-field effects into practical communication ranges. As a result, XL-MIMO systems depart from the far-field assumptions of conventional MIMO and instead operate in a regime dominated by spherical wavefronts.

Within the expanded near-field regime, the wireless channel exhibits enhanced spatial resolution and finer angular discrimination due to its spherical wave propagation. These unique physical characteristics provide the theoretical foundation for a range of frontier applications critical to 6G systems, such as high-precision user localization and tracking [4], and efficient adaptive beam management [5]. To effectively exploit these advantages in practice, it is highly beneficial to construct an accurate near-field radio map, which provides a powerful tool for modeling and leveraging the complexity of the near-field environment.

Specifically, the near-field radio map enables these advanced applications by characterizing the intricate spatial distribution of received signal strength (RSS) across both angle and distance. For user localization and tracking, the near-field radio map allows observed RSS patterns to be aligned with the map’s known distributions, achieving sub-meter positioning precision [4]. Moreover, its detailed angle-distance profiles directly support adaptive beam management strategies, providing the critical data needed to optimize beam steering and reduce the overhead of channel estimation and initial access in highly directional XL-MIMO systems [5].

Recent advances in radio map construction have spanned several categories, including interpolation-based methods, compressive sensing methods, tensor methods and learning-based methods. Interpolation-based methods include Kriging [6], [7] and kernel-based methods [8]–[12]. In [7], a space-frequency interpolation scheme was developed by introducing a linear shadowing interpolation across frequencies before applying spatial Kriging. A recent work [12] learned a set of kernel density functions to model the radio map using non-parametric estimation. Compressive sensing-based methods include sparse Bayesian learning [13]–[15], dictionary learning [16], and matrix completion [17]–[19]. The works in [13], [14] leveraged sparse Bayesian learning to reduce the number of required measurements while maintaining high reconstruction accuracy. In [15], gradient descent was combined with greedy matching to enhance sampling efficiency, followed by spatial-temporal semi-variogram modeling to facilitate accurate reconstruction. Tensor methods [20]–[26] have also been explored for high-dimensional radio map construction. Recent work [23] proposed an orthogonal matching pursuit based on a tensor structure to recover 3D spectrum map. The work in

Hao Sun and Xianghao Yu are with the Department of Electrical Engineering, City University of Hong Kong, Hong Kong (e-mail: hao.sun@cityu.edu.hk; alex.yu@cityu.edu.hk).

Junting Chen is with the School of Science and Engineering (SSE), Shenzhen Future Network of Intelligence Institute (FNii-Shenzhen), and Guangdong Provincial Key Laboratory of Future Networks of Intelligence, The Chinese University of Hong Kong, Shenzhen, Guangdong 518172, China (e-mail: juntingc@cuhk.edu.cn).

[25] leveraged canonical polyadic decomposition (CPD) to reconstruct spatial-spectral-temporal map. In parallel, learning-based methods have emerged as powerful tools for radio map construction [27]–[31]. In [28], a generative model combined with a tensor structure was proposed to extract underlying structures in the map. The authors in [29] developed a virtual obstacle model to characterize geometry-induced signal variation through neural networks. In [31], a novel generative framework leveraging conditional denoising diffusion probabilistic models was introduced to synthesize high-quality radio map from limited data. Beyond these, hybrid methods that combine interpolation with structure-informed modeling have gained increasing attention [32]–[37]. In [32], an uncertainty-aware matrix completion approach was proposed through integrating local polynomial regression (LPR) to improve radio map construction. The work in [33] utilized k -nearest neighbors Gaussian process regression to exploit spatial signal similarity. In [34], interpolation was incorporated with block-term tensor decomposition to reconstruct 3D map. A convex optimization framework that integrates interpolation with matrix completion was proposed in [36], which embeds interpolation into a low-rank matrix model and solves it using the alternating direction method of multipliers (ADMM).

However, most of these methods are not well-suited for near-field radio map construction due to the distinctive propagation characteristics in the near-field region. Unlike its far-field counterpart, near-field wavefronts exhibit strong dependence on both angle and distance, resulting in rapid spatial variations of signal strength and distinct radial symmetry around the antenna array. Nevertheless, since the RSS is determined by a small number of physical parameters, primarily range, azimuth, and the array layout, the resulting near-field radio map exhibits an approximately low-rank structure. Unfortunately, conventional reconstruction approaches typically fail to simultaneously exploit both local spatial correlations and the inherent global low-rank structure of near-field radio map, while learning-based methods require large amounts of labeled data and suffer from limited interpretability.

Addressing these challenges is hindered by two main issues. First, purely global low-rank models often neglect sharp, localized RSS variations, particularly near the transmitter, which in turn makes conventional uniform sampling highly inefficient by placing redundant samples in smooth regions while undersampling areas of rapid change. Second, existing hybrid methods that combine interpolation and matrix completion lack a systematic approach to determining the optimal balance between local interpolation accuracy and global completion consistency.

To address these limitations, we introduce a novel framework that jointly exploits the local variation and low-rank structures for near-field radio map construction. Our method uses regularized radial basis function (RBF) interpolation as a powerful prior to assist the matrix completion process. This RBF-assisted approach enables a theoretically-grounded, non-uniform sampling strategy that concentrates measurements where they are most needed. Furthermore, it incorporates a data-driven mechanism to adaptively balance the influence of the RBF model against the low-rank assumption, creating a

robust and accurate reconstruction.

The main contributions are summarized as follows:

- We develop a unified approach that amalgamates regularized RBF interpolation, which captures local near-field variations, with matrix completion that recovers the global low-rank structure of the near-field radio map. The regularized RBF model includes a constant term that improves reconstruction accuracy, especially around field boundaries.
- Motivated by theoretical RBF interpolation error analysis, which reveals the significance of measurement density and spatial signal variation, we propose an inverse μ -law-based non-uniform sampling strategy that places denser measurements in regions with sharp RSS variation (e.g., near the transmitter), thereby improving spatial resolution where it is most critical.
- We propose an adaptive parameter estimation strategy using robust Huberized LOOCV. By robustly estimating interpolation error from data-driven cross-validation, this method adaptively selects the tolerance parameter δ , ensuring an optimal balance between fidelity to the local RBF prior and enforcement of global low-rank structure.
- Our experiments find that the proposed RBF-driven matrix completion framework consistently outperforms traditional interpolation and matrix completion techniques. Regularized RBF interpolation achieves over 40% normalized mean squared error (NMSE) reduction at low sampling densities, while inverse μ -law sampling improves accuracy by over 10% compared to uniform sampling. The adaptive tolerance parameter selection via Huberized leave one out cross validation (LOOCV) further enhances reconstruction stability and performance. Overall, the method delivers more than 10% NMSE gain under various sampling and shadowing conditions.

The rest of the paper is organized as follows. Section II introduces the near-field channel model, describing the considered XL-MIMO system and the associated near-field signal propagation characteristics. Section III details our proposed solution in a step-by-step manner. It first presents the regularized RBF interpolation method for modeling local signal variations, followed by the inverse μ -law sampling strategy designed to optimize its accuracy. It then integrates this RBF-based prior into a global matrix completion model, introducing the Huberized LOOCV scheme as a robust mechanism for fusing the two components. The computational complexity of the proposed method is then analyzed. Section IV presents extensive simulation results, demonstrating the effectiveness and robustness of the proposed methods. Finally, conclusions are provided in Section V.

Notation: Scalars and sets are denoted by italic letters (e.g., x and \mathcal{X}). Bold italic lowercase letters (e.g., \mathbf{x}) denote vectors, and bold italic uppercase letters (e.g., \mathbf{X}) represent matrices. The entry at the i -th row and j -th column of matrix \mathbf{X} is denoted by X_{ij} . The symbol $\|\mathbf{X}\|_*$ refers to the nuclear norm, representing the sum of the singular values of matrix \mathbf{X} . The transpose and conjugate transpose are denoted by $(\cdot)^T$ and $(\cdot)^H$, respectively. \mathbb{R} and \mathbb{C} denote the sets of real and complex

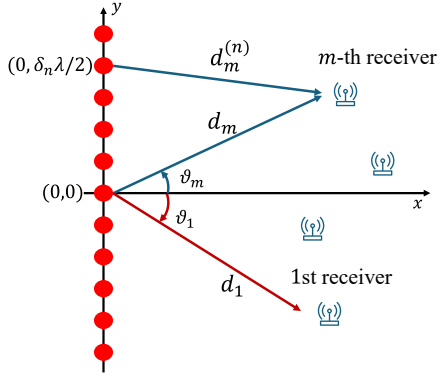


Figure 1. XL-MIMO near-field sensing scenario.

numbers, respectively. $\mathcal{N}(\mu, \sigma^2)$ and $\mathcal{CN}(\mu, \sigma^2)$ denote the real- and complex-valued Gaussian distributions with mean μ and variance σ^2 , respectively. j denotes the imaginary unit with $j^2 = -1$. $O(x)$ means $|O(x)|/x \leq C$, for all $x > x_0$ with C and x_0 are positive real numbers. The symbol $|\cdot|$ denotes the absolute value of a scalar argument (e.g., $|x|$) and the cardinality of a set argument (e.g., $|\mathcal{X}|$).

II. SYSTEM MODEL

Consider a downlink narrowband near-field XL-MIMO system as illustrated in Fig. 1. A transmitter equipped with N antennas, arranged in an extremely large uniform linear antenna array (ULA), serves a designated area. Assume there are M single antenna receivers. Without loss of generality (w.l.o.g.), the transmitter is positioned along the y -axis, with the n -th antenna located at $(0, \delta_n \lambda / 2)$, where $\delta_n = (2n - N - 1) / 2$ for $n = 1, 2, \dots, N$, $\lambda = c / f$ denotes the wavelength, f is the operating frequency, and c is the speed of light.

The received signal y_m at the m -th receiver is given by

$$y_m = \sqrt{P} \mathbf{h}_m^H \mathbf{v} s + n, \quad m = 1, 2, \dots, M, \quad (1)$$

where $P > 0$ is the transmit power, $\mathbf{h}_m \in \mathbb{C}^{N \times 1}$ is the downlink channel vector, and $\mathbf{v} \in \mathbb{C}^{N \times 1}$ denotes the transmit beamforming vector at the transmitter. The term s is the transmitted symbol, satisfying $\mathbb{E}[|s|^2] = 1$ w.l.o.g., and $n \sim \mathcal{CN}(0, \xi^2)$ denotes the additive receiver noise, where ξ^2 is the noise power.

The downlink channel steering vector $\mathbf{h}_m \in \mathbb{C}^{N \times 1}$ is modeled as

$$\mathbf{h}_m = \sqrt{\frac{N}{L}} \sum_{l=1}^L \beta_{l,m} \mathbf{a}(\vartheta_{l,m}, d_{l,m}), \quad (2)$$

where L denotes the number of paths, which include the line-of-sight (LOS) and non-line-of-sight (NLOS) paths. The parameter $\beta_{l,m}$ represents the path attenuation between the center of the antenna array and the m -th receiver along the l -th path, and $\mathbf{a}(\vartheta_{l,m}, d_{l,m})$ is the near-field array steering vector, where $\vartheta_{l,m}$ denotes the spatial angle from the center of the antenna array to the m -th receiver along the l -th path, and $d_{l,m}$ is the distance between the center of the antenna array and the m -th receiver along the l -th path.

Due to the large aperture of the XL-MIMO array and the resulting near-field propagation properties, the power of the NLOS paths is typically more than 20 dB weaker than that of the LOS path [3], [38]. Consequently, the LOS path typically dominates. Hence, w.l.o.g., we assume $L = 1$, simplifying the channel model (2) to

$$\mathbf{h}_m = \sqrt{N} \beta_m \mathbf{a}(\vartheta_m, d_m). \quad (3)$$

The path attenuation β_m of the LOS path, including the path loss and the shadowing effect, is modeled as

$$\beta_m = \frac{\lambda}{4\pi d_m} 10^{\varepsilon/20}, \quad (4)$$

where ε is a random variable accounting for the effect of shadowing in logarithmic (dB) scale with $\varepsilon \sim \mathcal{N}(0, \sigma^2)$.

Based on the spherical wavefront propagation model, the near-field array steering vector $\mathbf{a}(\vartheta_m, d_m)$ is given by

$$\mathbf{a}(\vartheta_m, d_m) = \frac{1}{\sqrt{N}} \left[e^{-j2\pi d_m^{(0)}/\lambda}, \dots, e^{-j2\pi d_m^{(N-1)}/\lambda} \right]^T, \quad (5)$$

where $d_m^{(n)}$ denotes the distance between the m -th receiver and the n -th antenna at the transmitter, computed as

$$d_m^{(n)} = \sqrt{d_m^2 + \delta_n^2 \lambda^2 / 4 - d_m \cos(\vartheta_m) \delta_n \lambda}. \quad (6)$$

In the dB scale, from (1)–(4), the RSS γ_m is then defined by

$$\begin{aligned} \gamma_m &= 10 \log_{10} \left(\left| \sqrt{P} \mathbf{h}_m^H \mathbf{v} s \right|^2 \right) \\ &= 10 \log_{10} \left(\left| \sqrt{\frac{P}{N}} \frac{\lambda}{4\pi d_m} \sum_{n=0}^{N-1} v_n e^{-j\frac{2\pi}{\lambda} d_m^{(n)}} s \right|^2 \right) + \varepsilon. \end{aligned} \quad (7)$$

To enable near-field radio-map construction, we discretize the region of interest into an angular-distance grid, yielding an $I \times J$ RSS matrix $\Gamma \in \mathbb{R}^{I \times J}$, where I and J are the numbers of quantized angular and radial points, respectively. Each cell (i, j) uniquely corresponds to a spatial angle θ_i and radial distance r_j . Let (i_m, j_m) denote the grid cell in which the m -th receiver lies, with spatial angle θ_{i_m} and radial distance r_{j_m} . In other words, the continuous angular ϑ_m and radial distance d_m of the m -th receiver are quantized to their discrete counterparts associated with cell (i_m, j_m) . The measured RSS γ_m at the m -th receiver is therefore assigned to cell (i_m, j_m) , i.e., $\Gamma_{i_m j_m} = \gamma_m$.

Our goal in this paper is to reconstruct the complete RSS matrix Γ using only sparse observations $\{(\theta_{i_m}, r_{j_m}, \Gamma_{i_m j_m})\}_{m=1}^M$ collected by a limited number of receivers.

III. STRUCTURE-AWARE RECOVERY FRAMEWORK

In this section, we introduce a structure-aware recovery framework for near-field radio map reconstruction that jointly exploits the local variation and global low-rank structures. Specifically, the proposed approach leverages a physics-informed prior derived via RBF interpolation, which is seamlessly integrated into a global low-rank matrix completion formulation. We first describe the overall recovery framework.

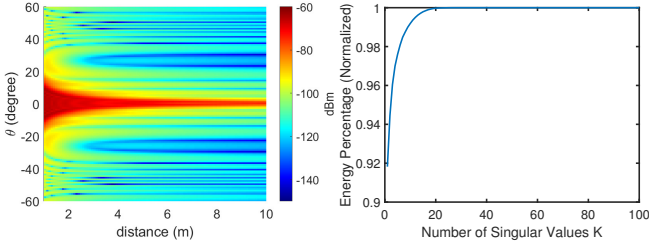


Figure 2. (a) Ground truth of near-field radio map. (b) Percentage of the sum of the first K dominant singular values over the sum of all singular values for a 100 by 100 near-field radio map matrix.

Then, we detail three critical components: (i) the construction of a high-fidelity local prior informed by near-field propagation physics, (ii) a theoretically grounded non-uniform sampling strategy that enhances construction accuracy, and (iii) an adaptive fusion mechanism that balances the local prior and global model via selection of the tolerance parameter.

A. Overall Formulation

Recall that $\Gamma \in \mathbb{R}^{I \times J}$ denotes the ground truth RSS matrix. There are sparse observations $\{\Gamma_{ij}\}$ available at a subset of entries, where the subscript m below i and j is omitted for notation simplicity. As illustrated in Fig. 2, the ground truth near-field RSS matrix exhibits a dominant low-rank structure with energy concentrated in a few singular values, thereby motivating the use of low-rank recovery. In addition to its low-rank nature, the RSS matrix also exhibits strong local correlations arising from the spatial continuity of radio signal propagation. To exploit both properties, we formulate a regularized nuclear norm minimization (NNM) problem as

$$\begin{aligned} & \underset{\mathbf{Z} \in \mathbb{R}^{I \times J}}{\text{minimize}} && \|\mathbf{Z}\|_* \\ & \text{subject to} && \hat{\Gamma} = f(\mathcal{P}_\Omega(\Gamma)) \\ & && |Z_{ij} - \hat{\Gamma}_{ij}| \leq \delta, \forall (i, j) \end{aligned} \quad (8)$$

where $\mathbf{Z} \in \mathbb{R}^{I \times J}$ is the optimization variable representing the reconstructed RSS matrix, and $\|\mathbf{Z}\|_*$ promotes a low-rank structure. $f(\mathcal{P}_\Omega(\Gamma))$ denotes an interpolation operator applied to the observations indexed by Ω with cardinality $|\Omega| = M$. The sampling operator $\mathcal{P}_\Omega: \mathbb{R}^{I \times J} \rightarrow \mathbb{R}^{I \times J}$ is defined by:

$$[\mathcal{P}_\Omega(\Gamma)]_{ij} = \begin{cases} \Gamma_{ij}, & (i, j) \in \Omega \\ \text{unknown}, & \text{otherwise} \end{cases}$$

The parameter $\delta > 0$ controls the fidelity of \mathbf{Z} to the interpolated prior $\hat{\Gamma}$. A small δ forces the recovered matrix to closely follow the interpolated prior, emphasizing local signal variations, whereas a large δ relaxes the constraint, allowing \mathbf{Z} to deviate from the prior and rely more heavily on NNM, thereby enhancing the enforcement of global low-rank structure. Therefore, an appropriate choice of δ is crucial for balancing local accuracy and global consistency.

The effectiveness of the proposed framework hinges on 1) the accurate construction of the prior $\hat{\Gamma}$ to reflect the spatial characteristics of near-field RSS; 2) the strategic selection of sampling locations to maximize measurement informativeness;

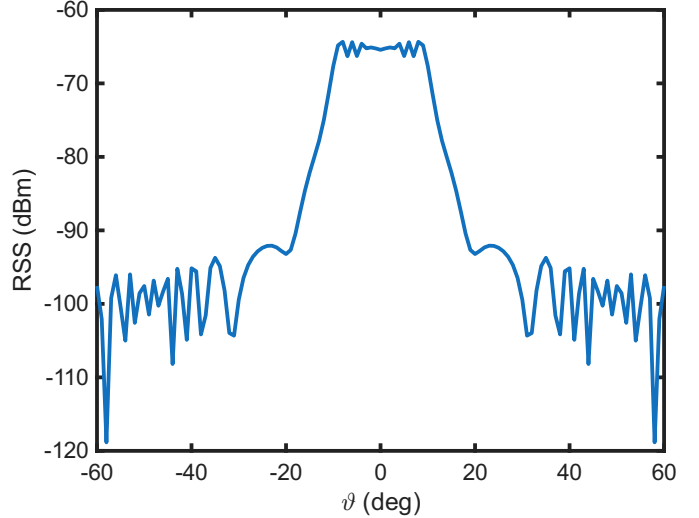


Figure 3. RSS versus direction ϑ at a fixed distance d . The RSS exhibits a sharp main lobe with multiple sidelobes.

3) and the data-driven yet theoretically grounded tuning of the fusion parameter δ , which governs the integration level between the interpolated prior and the recovered low-rank matrix. In the following, we shall present these three key design aspects.

B. Local Prior Construction via Regularized RBF Interpolation

In this subsection, we construct a high-fidelity interpolated prior $\hat{\Gamma}$ that captures the spatial characteristics of near-field RSS.

Direct interpolation over two-dimensional (2D) spatial domains typically requires dense sampling, since under spherical wave propagation, the RSS exhibits sharp variations along the angular direction, as illustrated in Fig. 3. To alleviate this issue, we conduct a near-field sensitivity analysis to justify adopting a 1D interpolation scheme along the radial direction, rather than performing full 2D interpolation that demands dense angular sampling.

We define the near-field array factor in (7) as $S(d, \vartheta) = \frac{\lambda}{4\pi d} \sum_{n=0}^{N-1} v_n e^{-j \frac{2\pi}{\lambda} d^{(n)}(d, \vartheta)}$.

Theorem 1 (Angular vs. Radial Sensitivity). *The partial derivatives of the near-field array factor magnitude $|S(d, \vartheta)|$ with respect to (w.r.t.) angular and radial perturbations satisfy*

$$\frac{\partial |S|}{\partial \vartheta} \leq \cos(\phi_\vartheta) \frac{5\lambda |\sin \vartheta|}{16d_{\min}} N^2 \quad (9)$$

$$\frac{\partial |S|}{\partial d} \leq \cos(\phi_d) \left(\frac{\lambda}{4\pi d^2} + \frac{1}{2d} \right) N, \quad (10)$$

where $\cos \phi_x$ is a phase-alignment factor and is independent of the array size N , d_{\min} represents the minimal distance from the measurement location to the array.

Proof. Please see Appendix A. \square

Theorem 1 characterizes the sensitivity of the near-field array factor magnitude $|S(d, \vartheta)|$ w.r.t. angular and radial

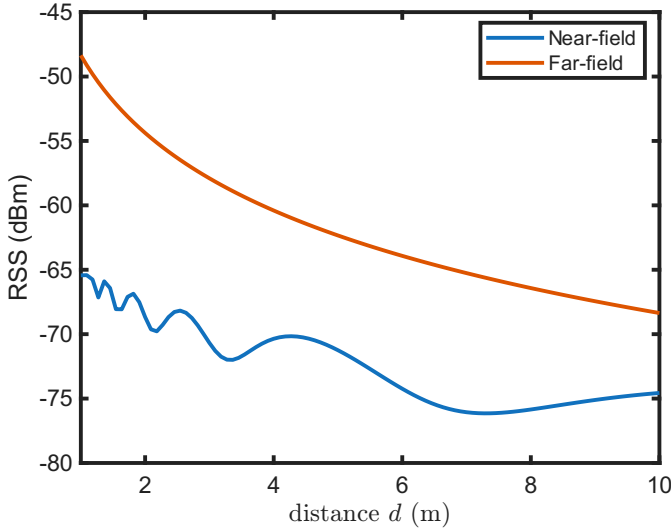


Figure 4. RSS versus distance d along a fixed spatial angle $\vartheta = 0^\circ$ under $N = 256$ antenna elements in the near- and far-field models. The near-field RSS exhibits more rapid fluctuations due to spherical wavefront effects, in contrast to the smoother decay observed in the approximation by far-field model.

perturbations, highlighting critical distinctions in their relative behavior.

Remark 1. Angular Sensitivity: The angular derivative exhibits an $O(N^2)$ envelope, scaled by $\lambda|\sin\vartheta|/(4d_{\min})$ and modulated by a phase-alignment factor $\cos\phi_\vartheta \in [-1, 1]$. Consequently, even small angular perturbations can induce large RSS fluctuations, consistent with the narrow main lobes and dense sidelobes in Fig. 3. Compared with the radial derivative (of order $O(N)$), the angular sensitivity grows faster with N , making angular interpolation the sampling bottleneck as N increases.

Remark 2. Radial Smoothness: In contrast, the radial derivative grows only linearly with N and decays smoothly with $1/d$, indicating much gentler RSS variations along the radial dimension. This is visually corroborated by Fig. 4, where the RSS changes gradually with distance. Hence, to cope with the severe angular sensitivity while maintaining manageable sampling overhead, we strategically perform one-dimensional interpolation along the radial direction for each fixed angle. This approach leverages the smoother radial structure to construct high-fidelity near-field radio maps without incurring excessive angular sampling burden.

Therefore, rather than performing full two-dimensional interpolation over the angular-radial domain, we focus on reconstructing RSS values along the radial dimension for each fixed spatial angle ϑ .

Let $\mathcal{S}_i = \{(\theta_i, r_j, \Gamma_{ij})\}$ denote the set of available measurements at a fixed spatial angle θ_i , where $j \in \Omega_i$. Here, $\Omega_i = \{j \mid (\theta_i, r_j, \Gamma_{ij}) \in \mathcal{S}_i\}$ represents the set of indices corresponding to radial measurement locations associated with the fixed spatial angle θ_i .

To capture the spatial variation of RSS along the radial dimension, an appropriate interpolation scheme is required. Classical methods such as LPR, and k -nearest neighbors

(KNN) rely on the choice of a local window size or the number of neighbors k . In LPR, the model order is also hard to choose: a low order yields lower accuracy, while a high order may overfit, hindering their effective use. RBF interpolation, by contrast, provides a flexible kernel-based framework; different kernels can be matched to different scenarios, and regularization offers robustness to noise. Therefore, to model the near-field RSS variation, we adopt a regularized RBF interpolation approach.

For each fixed angle θ_i , the RSS function $\rho_i(d)$ is modeled as

$$\rho_i(d) = \sum_{j=1}^{|\Omega_i|} \lambda_j \phi(|d - r_j|) + c, \quad (11)$$

where $\{\lambda_j\}$ are interpolation weights, $\phi(\cdot)$ is the RBF kernel (we use the multiquadric kernel, to be detailed in Section IV), and c is a constant term. The inclusion of c mitigates boundary errors and stabilizes the solution near domain edges.

To solve for the coefficients $\{\lambda_j\}$ and c in (11), we enforce the interpolation conditions

$$\rho_i(r_j) = \Gamma_{ij}, \quad j = 1, 2, \dots, |\Omega_i|, \quad (12)$$

together with the constraint

$$\sum_{j=1}^{|\Omega_i|} \lambda_j = 0 \quad (13)$$

to ensure uniqueness of the solution.

For computational efficiency, we reformulate these conditions using matrix notation. Let $|\Omega_i| = K$ and define the following variables:

- The RBF kernel matrix $\Phi \in \mathbb{R}^{K \times K}$, with entries

$$\Phi_{mn} = \phi(|r_m - r_n|). \quad (14)$$

- The measurement vector

$$\gamma_i = [\Gamma_{i1}, \Gamma_{i2}, \dots, \Gamma_{iK}]^T \in \mathbb{R}^K. \quad (15)$$

- The RBF coefficient vector

$$\lambda = [\lambda_1, \lambda_2, \dots, \lambda_K]^T \in \mathbb{R}^K, \quad (16)$$

- The all-one vector $\mathbf{1}_K = [1 \ 1 \ \dots \ 1]^T \in \mathbb{R}^K$.

Then, the interpolation conditions and the zero-sum constraint in (12) and (13) can be expressed compactly as the linear system:

$$\begin{bmatrix} \Phi & \mathbf{1}_K \\ \mathbf{1}_K^T & 0 \end{bmatrix} \begin{bmatrix} \lambda \\ c \end{bmatrix} = \begin{bmatrix} \gamma_i \\ 0 \end{bmatrix}. \quad (17)$$

Given that the multiquadric kernel is strictly positive definite, Φ is invertible. The solution can be expressed in closed form as

$$c = (\mathbf{1}_K^T \Phi^{-1} \mathbf{1}_K)^{-1} (\mathbf{1}_K^T \Phi^{-1} \gamma_i), \quad (18)$$

$$\lambda = \Phi^{-1} \left(\gamma_i - \mathbf{1}_K (\mathbf{1}_K^T \Phi^{-1} \mathbf{1}_K)^{-1} \mathbf{1}_K^T \Phi^{-1} \gamma_i \right). \quad (19)$$

C. Adaptive Sampling for RBF Interpolation

In this subsection, we allocate sampling locations to enhance interpolation accuracy under a fixed measurement budget. Due to spherical wave propagation, the near-field RSS exhibits steep radial gradients near the transmitter and smoother variations at larger distances. Combined with the RBF error bound, this motivates allocating more samples to regions with high variability. To this end, we develop a non-uniform sampling strategy based on the inverse μ -law transformation, which concentrates sampling density near the transmitter.

1) *Interpolation Error Bound Analysis:* To draw the theoretical grounded insight on the choice of sampling strategy, we analyze the interpolation error associated with multiquadric RBF. The following definitions and theorem establish a rigorous foundation for sampling strategy design.

Definition 1 (Fill Distance). Let $R = \{r_1, \dots, r_N\}$ be a set of points in a bounded domain \mathcal{D} . The fill distance h of R w.r.t. \mathcal{D} is defined as

$$h = \sup_{d \in \mathcal{D}} \min_{1 \leq j \leq N} |d - r_j|,$$

which quantifies how effectively the points in R cover the domain \mathcal{D} . Intuitively, the fill distance h represents the radius of the largest empty ball that can fit among the measurement points.

Definition 2 (Essentially Bounded). Let $f : \mathcal{D} \rightarrow \mathbb{R}$ be a measurable function. The essential supremum norm of f is defined as

$$\|f\|_{L_\infty(\mathcal{D})} = \inf \{C_0 \geq 0 : |f(d)| \leq C_0 \text{ a.e. on } \mathcal{D}\},$$

where ‘‘a.e.’’ denotes almost everywhere. This norm measures the smallest bound that holds almost everywhere in \mathcal{D} .

Let $\mathcal{N}_\phi(\mathcal{D})$ denote the native space of the reproducing kernel ϕ . The following theorem, adapted from [39], provides an upper bound for the interpolation error using RBF interpolation.

Theorem 2 (Error bound). Consider $\phi(d) = (1 + d^2)^\beta$, and define $f(d) = \phi(\sqrt{d})$. Then for every integer $\ell \geq \lceil \beta \rceil$, the ℓ th derivative of f satisfies

$$|f^{(\ell)}(d)| \leq \ell! C_1^\ell, \quad \forall d \geq 0, \quad (20)$$

where $C_1 = (1 + d)^{\beta/\ell-1} (1 + |\beta + 1|)$ is a constant.

In addition, there exists a constant $c > 0$ such that for any sufficiently small fill distance h , the interpolation error between a function $f \in \mathcal{N}_\phi(\mathcal{D})$ and its interpolant ρ is bounded by

$$\|f - \rho\|_{L_\infty(\mathcal{D})} \leq e^{-c/h} |f|_{\mathcal{N}_\phi(\mathcal{D})},$$

where $|\cdot|_{\mathcal{N}_\phi(\mathcal{D})}$ is the native seminorm, closely related to the magnitude of higher-order derivatives of f .

Proof. Please see Appendix B. \square

Since the multiquadric RBF chosen in (11) is precisely of the form $\phi(d) = (1 + \epsilon d^2)^\beta$ with $\beta = 1/2$ and $\epsilon = 1$, Theorem 2 becomes directly applicable, thereby providing

explicit interpolation error bounds for the multiquadric RBF interpolation.

We highlight two critical insights from this error analysis in the following.

Remark 3. The interpolation error bound derived in Theorem 2 indicates that as RSS measurements become denser, i.e., $h \rightarrow 0$, interpolation error decreases exponentially. Therefore, RBF interpolation can achieve high accuracy if the measurements are sufficiently dense. Consequently, the fill distance h directly governs the achievable interpolation accuracy.

Remark 4. If the near-field RSS function exhibits pronounced spatial variability, the seminorm $|f|_{\mathcal{N}_\phi(\mathcal{D})}$ increases, leading to higher interpolation errors. One effective strategy to mitigate this is to reduce the fill distance h by increasing the measurement density. However, in practical settings where the number of measurements is constrained, a more feasible solution is to adopt a non-uniform sampling strategy. This strategy allocates more samples to regions with high signal variation and fewer samples to smoother regions, thereby optimizing accuracy under a limited measurements.

2) *Inverse μ -Law Non-Uniform Sampling:* Motivated by the preceding error analysis and the observation that near-field RSS exhibits steep gradients near the transmitter and smoother variations at greater distances, we propose a non-uniform sampling strategy based on the inverse μ -law transformation. This approach effectively concentrates samples near the transmitter, where the interpolation error is most sensitive to spatial resolution.

Given a scalar input $x \in [0, 1]$ and a companding parameter $\mu > 0$, the μ -law transformation $F(x)$ is defined as

$$F(x) = \frac{\ln(1 + \mu x)}{\ln(1 + \mu)}. \quad (21)$$

Directly applying the forward μ -law transformation compresses the lower portion of the domain and stretches the upper portion. However, this contradicts the spatial requirements in near-field scenarios, where higher resolution is needed near the transmitter (i.e., at the lower end of the spatial domain). To address this issue, we instead employ the inverse μ -law transformation:

$$F^{-1}(y) = \frac{(1 + \mu)^y - 1}{\mu}, \quad y \in [0, 1],$$

which maps uniformly spaced values y into a set of samples that are concentrated near zero.

The non-uniform sampling procedure is implemented as follows:

- Generate N independent uniform samples $u_i \sim \mathcal{U}(0, 1)$, uniformly distributed over $[0, 1]$.
- Apply the inverse μ -law transformation to obtain

$$y_i = \frac{(1 + \mu)^{u_i} - 1}{\mu}. \quad (22)$$

- Map the transformed samples $y_i \in [0, 1]$ to the target spatial interval $[z_0, z_1]$ via linear scaling:

$$r_i = z_0 + y_i(z_1 - z_0). \quad (23)$$

The resulting spatial sample set $\{r_i\}$ is thus non-uniformly distributed over $[z_0, z_1]$, with a concentration of samples near z_0 , i.e., in close proximity to the transmitter.

The clustering effect is controlled by the parameter μ , where larger values yield stronger concentration near the lower end of the domain. This non-uniform allocation efficiently reduces interpolation error in regions with high RSS variability while maintaining overall sampling efficiency.

D. Adaptive Fusion of RBF Prior and Low-Rank Model

In this subsection, we effectively fuse the RBF-interpolated prior with the global low-rank structure discussed in (8) to ensure robust reconstruction. In practice, excessive reliance on the RBF prior may propagate local interpolation errors, while an overly loose constraint may disregard informative local variations. The tolerance parameter δ governs this trade-off by controlling the allowable deviation from the prior. We embed the RBF prior as inequality constraints in an NNM problem and adaptively determine δ through a Huberized LOOCV procedure.

1) *Integration of RBF Prior into Low-Rank Recovery:* Classical matrix completion methods leverage the assumption that the underlying data matrix is low-rank, aiming to recover it from a small subset of observed entries.

After constructing the prior $\hat{\Gamma}$, we integrate it into the low-rank recovery framework. This involves solving the main optimization problem (8) and adaptively setting the tolerance parameter δ . Based on the RBF interpolation result, (8) can be reformulated as:

$$\begin{aligned} & \underset{\mathbf{Z}}{\text{minimize}} \quad \|\mathbf{Z}\|_* \\ & \text{subject to} \quad |Z_{ij} - \hat{\Gamma}_{ij}| \leq \delta, \quad \forall(i, j) \\ & \quad \hat{\Gamma}_{ij} = \sum_{k \in \Omega_i} \lambda_{i,k} \phi_{j,k} + c_i \\ & \quad \lambda_i = \Phi_i^{-1} \left(\gamma_i - \mathbf{1}_K (\mathbf{1}_K^T \Phi_i^{-1} \mathbf{1}_K)^{-1} \mathbf{1}_K^T \Phi_i^{-1} \gamma_i \right) \\ & \quad c_i = (\mathbf{1}_K^T \Phi_i^{-1} \mathbf{1}_K)^{-1} (\mathbf{1}_K^T \Phi_i^{-1} \gamma_i). \end{aligned} \quad (24)$$

Here, $\phi_{j,k}$ denotes the radial basis function evaluated at location r_j with respect to center r_k , and δ controls the allowable deviation between the recovered matrix \mathbf{Z} and the RBF prior. The coefficients c_i and λ_i are from (18)–(19).

The resulting problem (24) is a convex optimization program comprising a nuclear norm objective and linear inequality and equality constraints. It can be efficiently solved using the standard interior point method [40].

2) *Adaptive Parameter Selection via Huberized LOOCV:* The tolerance parameter δ plays a pivotal role in balancing the influence of the RBF prior and the global low-rank constraint. A small δ may lead to overfitting to the prior, whereas a large δ may cause the recovery to ignore valuable local structure.

To automatically determine a proper δ , a Huberized LOOCV approach is proposed. In standard LOOCV, each observation is removed from the training set in turn; the model is then refitted using the remaining samples, and the prediction at the held-out location yields an out-of-sample error. Specifically, we apply

LOOCV to the RBF interpolation and obtain a sequence of prediction errors $\{e_k\}_{k=1}^K$, where each error e_k is defined as

$$e_k = \Gamma_{ik} - \rho_{i,-k}(r_k), \quad (25)$$

where $\rho_{i,-k}(r_k)$ denotes the interpolant constructed by excluding the k -th measurement from the dataset $\mathcal{S}_i = \{(\theta_i, r_j, \Gamma_{ij})\}$. The interpolant is defined as

$$\rho_{i,-k}(r_k) = \sum_{j=1, j \neq k}^K \lambda_j \phi(\|r_k - r_j\|) + c,$$

where the coefficients λ_j and constant c are computed using the same interpolation procedure described in (17)–(19), but based only on the reduced measurement set $\Omega_i \setminus \{k\}$.

To calibrate the tolerance δ , we estimate a robust typical error level from the LOOCV residuals using the Huber estimator. This choice yields a stable summary for δ while preventing a few large residuals from dominating.

Let $\{e_k\}_{k=1}^K$ denote the LOOCV errors. The Huber estimator $\hat{\mu}$ is defined as the minimizer of the aggregated Huber loss:

$$\hat{\mu} = \arg \min_{\mu \in \mathbb{R}} \sum_{k=1}^K g(e_k - \mu), \quad (26)$$

where $g(\cdot)$ is the Huber loss function given by

$$g(r) = \begin{cases} \frac{1}{2}r^2, & |r| \leq \varsigma_H, \\ \varsigma_H(|r| - \frac{1}{2}\varsigma_H), & |r| > \varsigma_H, \end{cases} \quad (27)$$

and $\varsigma_H > 0$ is a threshold that controls the transition from a quadratic penalty to a linear penalty. Equation (26) can be solved via an iterative re-weighted least squares procedure. In iteration t , we update

$$\mu^{(t+1)} = \frac{\sum_{k=1}^K w_k^{(t)} e_k}{\sum_{k=1}^K w_k^{(t)}}, \quad (28)$$

where

$$w_k^{(t)} = \begin{cases} 1, & \text{if } |e_k - \mu^{(t)}| \leq \varsigma_H, \\ \frac{\varsigma_H}{|e_k - \mu^{(t)}|}, & \text{otherwise.} \end{cases} \quad (29)$$

Upon convergence, we set the tolerance based on this robust center, $\delta = \hat{\mu}$. This data-driven choice ties δ to the observed out-of-sample interpolation error of the RBF prior, avoiding both overfitting and underfitting.

E. Complexity Analysis

The proposed RBF-driven matrix completion method consists of two main components: (i) a regularized RBF interpolation stage and (ii) an NNM-based matrix completion stage. Each component has distinct computational characteristics.

Let I and J denote the angular and radial resolutions of the reconstructed radio map, respectively, i.e., the target RSS matrix is $\mathbf{Z} \in \mathbb{R}^{I \times J}$. Interpolation is performed independently along each angular slice θ_i , for $i = 1, 2, \dots, I$ with Ω_i represents the set of available measurement indices at angle θ_i , and assume $|\Omega_i| = K \ll J$. For each θ_i , constructing the

RBF kernel matrix $\Phi \in \mathbb{R}^{K \times K}$ requires $O(K^2)$ operations. Solving the linear system in (17) to obtain (λ, c) requires $O(K^3)$ operations. Thus, across all I angular directions, the total interpolation cost is $O(IK^3)$.

To refine the interpolated map, we solve the NNM-based matrix completion problem (24), where the interpolated values serve as soft constraints. For an $I \times J$ matrix, the completion cost is: $O((I+J) \log^3(I+J))$ [41]. The tolerance parameter δ is selected via the Huberized LOOCV method. This requires re-solving the interpolation K times per angular slice, resulting in an overall LOOCV complexity of $O(IK^4)$.

Hence, the total computational complexity of the proposed method is $O(IK^4 + (I+J) \log^3(I+J))$.

The overall complexity is essentially the additive combination of the baseline RBF interpolation and matrix completion modules, each offering complementary benefits in terms of spatial modeling capabilities.

IV. SIMULATION RESULTS

We evaluate the performance of the proposed RBF-assisted matrix completion method under a near-field millimeter-wave XL-MIMO scenario. Unless stated otherwise, all simulations are performed under the following settings.

A. Simulation Setup

The transmitter is equipped with a ULA of $N = 256$ antennas, with an inter-element spacing of $\lambda/2 = 0.0015$ m. This results in a total aperture of $D = N\lambda/2 = 0.384$ m. The carrier frequency is $f = 100$ GHz (wavelength $\lambda = 0.003$ m), yielding a Rayleigh distance of $Z = 2D^2/\lambda \approx 98.3$ m. The ULA is aligned with the y-axis and centered at the origin. The transmitter transmits a unit-power symbol $s = 1$, and the total transmit power is normalized to $P = 1$. We consider an omnidirectional beamformer $\mathbf{v} = \frac{1}{\sqrt{N}}\mathbf{1}_N$ to focus on the spatial distribution of RSS.

The area of interest spans angles $\theta \in [-80^\circ, 80^\circ]$ and radial distances $r \in (0, 10]$ m. This domain is uniformly discretized into an $I \times J$ grids with $I = J = 100$. The ground-truth RSS matrix, \mathbf{Z} , is generated according to (7), incorporating a shadowing component with standard deviation $\sigma \in [1, 4]$ dB. The path gain β_m and element-wise distances $\{d_m^{(n)}\}$ are computed using the spherical wavefront model as defined in (4) and (6), respectively.

We quantify the performance of the near-field radio map reconstruction using the NMSE, defined as:

$$\text{NMSE} = \frac{\|10^{\mathbf{Z}/10} - 10^{\hat{\mathbf{Z}}/10}\|_F^2}{\|10^{\mathbf{Z}/10}\|_F^2}, \quad (30)$$

where \mathbf{Z} and $\hat{\mathbf{Z}}$ are the ground-truth and estimated RSS matrices in decibels (dB), respectively, and $\|\cdot\|_F$ denotes the Frobenius norm.

In the proposed method, the tolerance parameter δ in (24) is automatically determined via the robust Huberized LOOCV scheme, with the Huber threshold ς_H set to the median absolute deviation of the LOOCV residuals $\varsigma_H = \text{median}(|e_i - \text{median}(e_j)|)$.

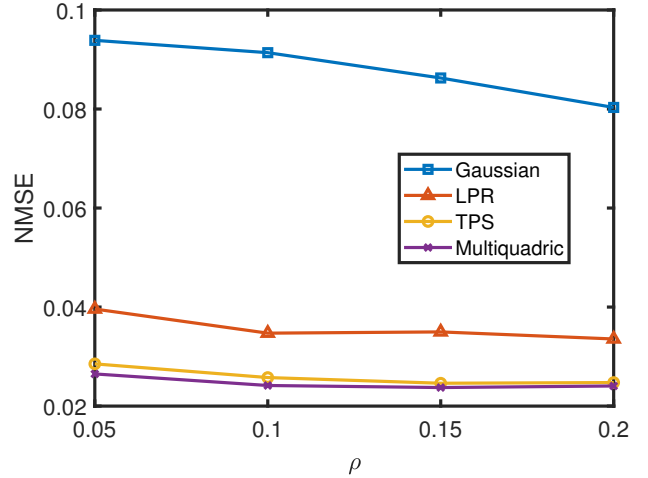


Figure 5. Reconstruction NMSE versus sampling ratio for different interpolation methods. The Quadratic RBF outperforms TPS, Gaussian RBF and LPR, particularly at low sampling ratios.

We compare the proposed approach against four baselines:

- **RBF Interpolation:** This method applies multiquadric RBF interpolation to each angular slice independently to estimate the missing RSS values, without leveraging global matrix structure.
- **Matrix Completion via NNM (MC-NNM)** [42]: A standard matrix completion approach that solves (24) using NNM without RBF-based interpolation prior.
- **Local Polynomial Regression (LPR):** A first-order local polynomial model [43], [44] with a Gaussian weighting kernel.
- **LPR-assisted Matrix Completion (LPR-MC):** A two-stage method where missing RSS values are first estimated using LPR, followed by a refinement step via an NNM-based matrix completion algorithm [32], [34].

B. Analysis of RBF Kernel Selection

We first validate the design choices for our RBF interpolation module.

We compare four interpolation schemes: multiquadric RBF ($\phi(d) = \sqrt{1 + \epsilon d^2}$ with $\epsilon = 1$), Gaussian RBF ($\phi(d) = \exp(-\epsilon d^2)$), thin plate spline (TPS) ($\phi(d) = d^2 \log d$), and LPR. Interpolation is performed on the radial dimension given each angle, using a uniformly sampled subset of measurements. To ensure a fair comparison, hyperparameters for all four interpolation schemes are carefully tuned. In particular, the LPR adopts a first-order local polynomial model with a Gaussian kernel for weighting.

Fig. 5 plots the reconstruction NMSE versus the sampling ratio $\rho = 0.05 - 0.2$. The multiquadric RBF consistently outperforms the other kernels, particularly at low sampling ratios. Unlike the overly smooth Gaussian and TPS kernels, it effectively balances smoothness with the ability to capture sharp local variations, justifying its use in our framework.

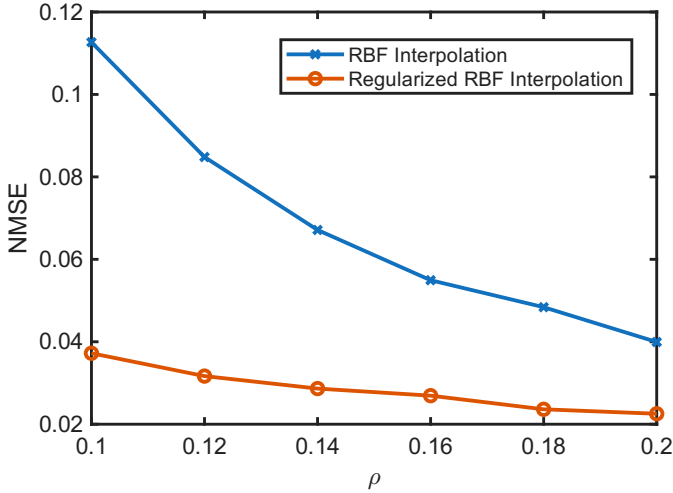


Figure 6. Comparison of reconstruction NMSE versus sampling ratio ρ for regularized and non-regularized RBF interpolation. The proposed regularization achieves substantial gains at low sampling densities by improving stability and extrapolation robustness.

C. Effectiveness of the Regularized RBF Interpolation

We now examine the performance gain brought by the proposed regularized RBF interpolation introduced in (11). We randomly sample a subset of entries in each row of the ground-truth RSS matrix \mathbf{Z} , with the sampling ratio ρ ranging from 0.1 to 0.2.

Fig. 6 compares the reconstruction NMSE of the standard RBF interpolation and the proposed regularized RBF interpolation across different sampling ratios. The results clearly show that the regularized RBF consistently achieves lower NMSE over all sampling regimes, yielding more than 40% NMSE reduction compared to the unregularized baseline.

This performance improvement is primarily attributed to the inclusion of a constant term in the RBF formulation. Without this term, the RBF interpolant must implicitly capture both local variations and the global offset of the signal. This can lead to instability and overfitting, especially near the boundaries or in regions with sparse observations. By decoupling the global offset (handled by the constant term) from local fluctuations (modeled by the RBFs), the regularized interpolation becomes more robust and accurate, especially in extrapolation-prone areas.

D. Performance of the Proposed Inverse μ -Law-Inspired Non-Uniform Sampling

In this subsection, we evaluate the effectiveness of the proposed inverse μ -law-inspired non-uniform sampling strategy for near-field RSS interpolation. The sampling ratio $\rho = M/(I \times J)$ is fixed at 0.1, indicating that only 10% of the RSS measurements over the angular-distance domain are available for interpolation. To model the effect of shadowing, we inject $\varepsilon \sim \mathcal{N}(0, \sigma^2)$ into the RSS values as defined in (7), and vary the standard deviation σ from 1 dB to 4 dB. We adopt a companding parameter $\mu = 15$ for the inverse μ -law transformation to achieve a dense sampling distribution near the transmitter.

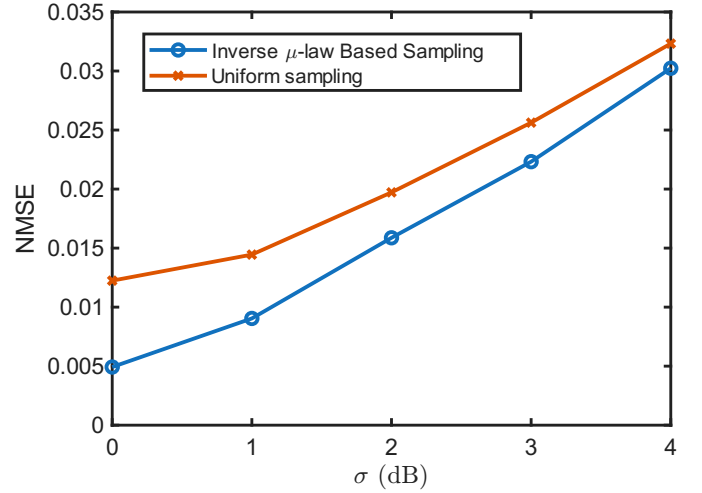


Figure 7. Comparison of reconstruction NMSE versus RSS shadowing condition σ under uniform sampling and inverse μ -law-inspired non-uniform sampling. The proposed non-uniform sampling strategy consistently achieves lower NMSE, particularly under low to moderate shadowing.

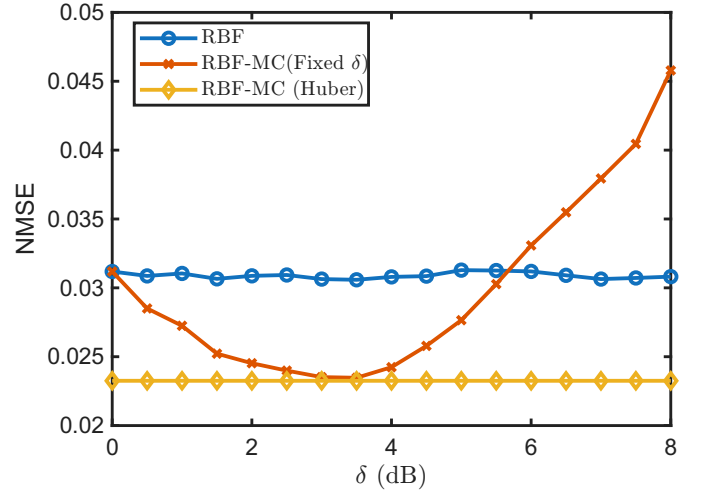


Figure 8. Comparison of reconstruction NMSE versus tolerance parameter δ for three methods: RBF interpolation (blue), RBF-driven matrix completion with fixed δ (red), and the proposed RBF-driven matrix completion using Huberized LOOCV for automatic δ estimation (yellow).

Fig. 7 presents the reconstruction NMSE under both uniform and inverse μ -law-inspired non-uniform sampling strategies. Across all shadowing conditions, the proposed method significantly outperforms the uniform baseline, achieving more than 10% reduction in NMSE. This improvement is attributed to the fact that the inverse μ -law transformation allocates more sampling points in regions of rapid signal variation, such as, near the transmitter, where the RSS changes more abruptly due to spherical wavefront propagation. In contrast, uniform sampling may waste measurements in smoother regions, leading to higher interpolation error in critical areas.

As σ increases, the NMSE under both sampling schemes rises due to the growing impact of the shadowing effect on the measurements. Nevertheless, the proposed non-uniform strategy maintains its advantage, demonstrating better robustness to the shadowing effect.

These results confirm that the proposed inverse μ -law-inspired sampling approach can efficiently allocate limited measurement resources and substantially enhance interpolation accuracy.

E. Performance of the Huberized LOOCV δ Estimate

We examine the impact of the tolerance parameter δ in the proposed RBF-driven matrix completion framework and demonstrate the effectiveness of using the Huberized LOOCV scheme for automatically δ estimation. The sampling ratio is fixed at $\rho = 0.2$, and the shadowing standard deviation is set to $\sigma = 4$.

To assess sensitivity, we vary the tolerance parameter δ in the matrix completion problem (24) from 0 to 8. The resulting reconstruction NMSE for fixed- δ configurations is shown as the red curve in Fig. 8. The performance clearly exhibits a strong dependence on the choice of δ : excessively small values result in overfitting to noisy RBF interpolants, while excessively large values fail to enforce meaningful agreement between the matrix completion output and the RBF estimates. An optimal range for δ exists, but identifying it manually is challenging and data-dependent.

To mitigate this issue, we employ the Huberized LOOCV method proposed in Section III-D to automatically determine a robust δ . The result of this method is shown as the yellow curve in Fig. 8, which appears flat across all δ values because δ is internally estimated rather than externally set. The performance is consistently superior to both the RBF interpolation (blue curve) and most fixed- δ settings, validating the effectiveness and robustness of the Huberized estimator.

These results confirm that (i) the performance of RBF-driven matrix completion is highly sensitive to the δ parameter, and (ii) the proposed Huberized LOOCV estimator offers a principled and robust way to automatically select δ , avoiding manual tuning and enhancing reconstruction accuracy.

F. Performance of the Proposed RBF-Driven Matrix Completion Under Different Sampling Ratios and Shadowing Conditions

In this subsection, we evaluate the performance of the proposed RBF-driven matrix completion method under varying sampling ratios and shadowing conditions, comparing it with four baseline approaches.

Fig. 9 illustrates the reconstruction NMSE as a function of the sampling ratio ρ , ranging from 0.06 to 0.16, with a fixed shadowing standard deviation $\sigma = 3$. The proposed method consistently outperforms all baselines, achieving more than a 10% improvement in NMSE at moderate to high sampling ratios. However, at very low sampling ratios, the scarcity of measurements adversely affects the accuracy of the Huberized LOOCV-based parameter estimation, leading to a degradation in reconstruction performance.

Next, we evaluate the robustness of the proposed method against the shadowing effect. Fig. 9 illustrates the reconstruction NMSE as a function of the shadowing standard deviation σ , which varies from 1 to 5, with the sampling ratio fixed at $\rho = 0.1$. The proposed method consistently outperforms

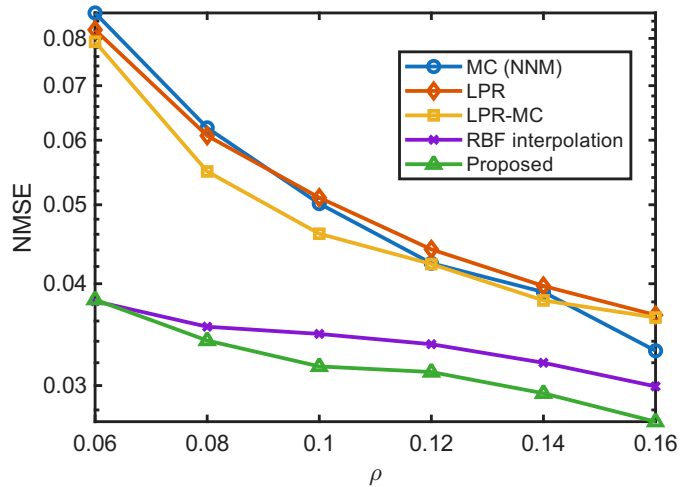


Figure 9. Reconstruction NMSE versus sampling ratio ρ . The proposed RBF-driven matrix completion method consistently achieves the lowest NMSE across all sampling ratios. Notably, it offers more than 10% improvement compared to baseline methods when the sampling ratio is moderate.

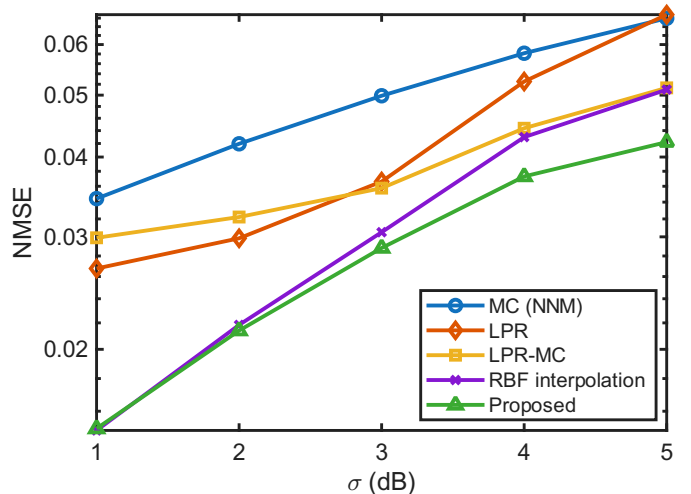


Figure 10. Reconstruction NMSE versus shadowing standard deviation σ . The proposed method consistently achieves the lowest NMSE across varying shadowing levels, demonstrating strong robustness to the shadowing effect.

all baseline approaches across the entire range of shadowing conditions, achieving more than a 10% improvement in NMSE even under severe shadowing. This robustness is attributed to the Huberized LOOCV-based selection of the tolerance parameter, which effectively integrates RBF interpolation with matrix completion. By leveraging both local smoothness and the global low-rank structure, the proposed method significantly mitigates the impact of outliers in noisy measurements.

These results confirm the effectiveness of the proposed framework in leveraging both spatial smoothness and low-rank structure, and its robustness to practical challenges such as sparse sampling and the shadowing effect.

To qualitatively assess reconstruction accuracy, we present a visual comparison of the recovered near-field radio map under a sampling ratio $\rho = 0.1$ and shadowing $\sigma = 4$ dB. As shown in Fig. 11, the proposed method exhibits the closest resemblance to the ground truth, with sharper spatial features

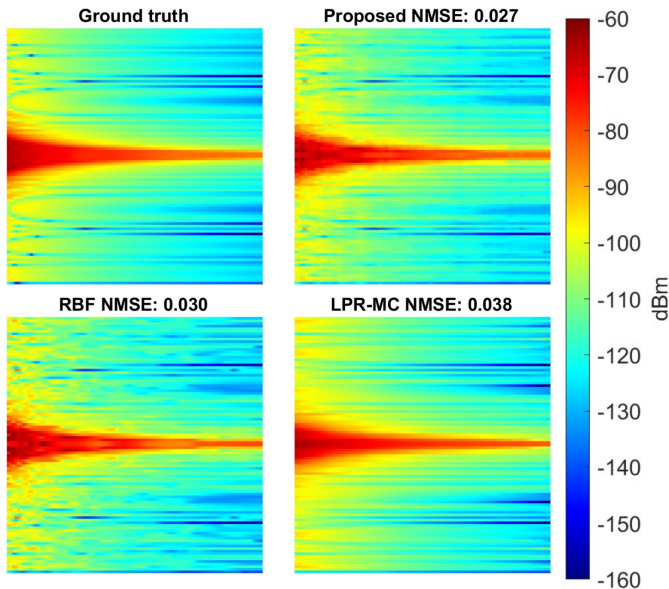


Figure 11. Visual comparison of reconstruction performance at sampling ratio $\rho = 0.1$ and shadowing $\sigma = 4$ dB. The horizontal axis represents the distance d , and the vertical axis represents the angular direction ϑ .

and reduced artifacts compared to the baseline approaches.

V. CONCLUSION

In this paper, we proposed a novel structure-aware RBF-assisted matrix completion framework tailored explicitly for near-field radio map reconstruction in millimeter-wave XL-MIMO systems. Our approach effectively integrates local spatial variations through a regularized RBF interpolation with a global low-rank structure via NNM, significantly outperforming conventional techniques. The introduction of a constant term in the regularized RBF interpolation notably enhanced accuracy near the boundaries, overcoming the limitations prevalent in standard interpolation methods. Leveraging theoretical interpolation error analysis, an adaptive inverse μ -law-inspired non-uniform sampling strategy is designed to optimally allocate measurement points, focusing sampling density in areas with rapid RSS variations near the transmitter. Moreover, a robust Huberized LOOCV scheme is introduced to adaptively select the tolerance parameter, effectively bridging local spatial correlation from RBF interpolation and global low-rank characteristics inherent in matrix completion. Extensive simulation results validated the superior performance and robustness of the proposed method, achieving more than 10% improvement in NMSE compared to existing interpolation and matrix completion techniques under various sampling densities and shadowing conditions.

APPENDIX A PROOF OF THEOREM 1

Given the near-field array factor

$$S(d, \vartheta) = \frac{\lambda}{4\pi d} \sum_{n=0}^{N-1} v_n e^{-j\frac{2\pi}{\lambda} d^{(n)}(d, \vartheta)},$$

where

$$d^{(n)}(d, \vartheta) = \sqrt{d^2 + \delta_n^2 \lambda^2 / 4 - d\delta_n \lambda \cos \vartheta},$$

we analyze the sensitivity of $|S(d, \vartheta)|$ w.r.t. both the radial distance d and angle ϑ . At certain critical points where the phase contributions from all array elements precisely cancel each other (i.e., $S(d, \vartheta) = 0$), the magnitude $|S(d, \vartheta)|$ becomes non-differentiable, despite $S(d, \vartheta)$ itself remaining smooth. In the following derivation, unless otherwise noted, we consider the differentiable region only.

We first show that $S(d, \vartheta)$ is smooth in both d and ϑ . The expression $d^{(n)}$ involves a square root of a quadratic polynomial, which is smooth because $d^{(n)}(d, \vartheta)$ represents the distance from n th antenna to the receiver. The function

$$g_n(d, \vartheta) = -j\frac{2\pi}{\lambda} d^{(n)}(d, \vartheta)$$

is a smooth composition of the linear factor $-j\frac{2\pi}{\lambda}$ and the smooth square root, and hence is smooth itself. Consequently, the complex exponential $f_n(d, \vartheta) = e^{g_n(d, \vartheta)}$ is also smooth by the chain rule. Since $S(d, \vartheta)$ is a finite sum of smooth functions, $S(d, \vartheta) = \sum_{n=0}^{N-1} f_n(d, \vartheta)$, it follows that $S(d, \vartheta) \in C^\infty$, i.e., it is infinitely differentiable in both d and ϑ .

Then, we perform the derivative of $S(d, \vartheta)$ w.r.t. both d and ϑ . The angular derivative of $S(d, \vartheta)$ w.r.t. ϑ is computed as

$$\frac{\partial S}{\partial \vartheta} = -\frac{j}{2d} \sum_{n=0}^{N-1} v_n \frac{\partial d^{(n)}}{\partial \vartheta} e^{-j\frac{2\pi}{\lambda} d^{(n)}}.$$

Taking the magnitude, we have

$$\begin{aligned} \left| \frac{\partial S}{\partial \vartheta} \right| &\leq \left| -\frac{j}{2d} \sum_{n=0}^{N-1} |v_n| \left| \frac{\partial d^{(n)}}{\partial \vartheta} \right| \left| e^{-j\frac{2\pi}{\lambda} d^{(n)}} \right| \right| \\ &\leq \frac{\max_n |v_n|}{2d} \sum_{n=0}^{N-1} \left| \frac{\partial d^{(n)}}{\partial \vartheta} \right| \\ &\leq \frac{1}{2d} \sum_{n=0}^{N-1} \left| \frac{\partial d^{(n)}}{\partial \vartheta} \right|. \end{aligned}$$

Since $\partial d^{(n)}/\partial \vartheta = d\lambda\delta_n/2/d^{(n)} \sin \vartheta$ and δ_n typically grows linearly with n , we have

$$\left| \frac{\partial S}{\partial \vartheta} \right| \leq \frac{\lambda |\sin \vartheta|}{4} \sum_{n=0}^{N-1} |\delta_n|/d^{(n)}.$$

Define $d_{\min} = \min_n d^{(n)}$. Since $\sum_{n=0}^{N-1} |\delta_n| \leq N^2/4 + 1$, then

$$\left| \frac{\partial S}{\partial \vartheta} \right| \leq \frac{\lambda |\sin \vartheta|}{16d_{\min}} (N^2 + 4) \leq \frac{5\lambda |\sin \vartheta|}{16d_{\min}} N^2,$$

since $N > 1$.

The derivative over distance d is given by

$$\begin{aligned} \frac{\partial S}{\partial d} &= -\frac{\lambda}{4\pi d^2} \sum_{n=0}^{N-1} v_n e^{-j\frac{2\pi}{\lambda} d^{(n)}} \\ &\quad - \frac{1}{2d} j \sum_{n=0}^{N-1} v_n \frac{\partial d^{(n)}}{\partial d} e^{-j\frac{2\pi}{\lambda} d^{(n)}}, \end{aligned} \quad (31)$$

with $\partial d^{(n)}/\partial d = (2d - \delta_n \lambda \cos \vartheta)/(2d^{(n)})$.

Taking the magnitude, we have

$$\begin{aligned} \left| \frac{\partial S}{\partial d} \right| &\leq \left| \frac{\lambda}{4\pi d^2} \sum_{n=0}^{N-1} v_n e^{-j\frac{2\pi}{\lambda} d^{(n)}} \right| \\ &\quad + \left| \frac{1}{2d} \sum_{n=0}^{N-1} v_n \frac{\partial d^{(n)}}{\partial d} e^{-j\frac{2\pi}{\lambda} d^{(n)}} \right|, \\ &< \frac{\lambda N}{4\pi d^2} + \left| \frac{1}{2d} \sum_{n=0}^{N-1} v_n \frac{2d - \delta_n \lambda \cos \vartheta}{2d^{(n)}} e^{-j\frac{2\pi}{\lambda} d^{(n)}} \right| \end{aligned} \quad (32)$$

Nest, we focus on bounding the second term $\left| \frac{1}{2d} \sum_{n=0}^{N-1} v_n \frac{2d - \delta_n \lambda \cos \vartheta}{2d^{(n)}} e^{-j\frac{2\pi}{\lambda} d^{(n)}} \right|$.

Applying the triangle inequality and using the bound $|v_n| \leq 1$, we have:

$$\begin{aligned} &\left| \frac{1}{2d} \sum_{n=0}^{N-1} v_n \frac{2d - \delta_n \lambda \cos \vartheta}{2d^{(n)}} e^{-j\frac{2\pi}{\lambda} d^{(n)}} \right| \\ &\leq \frac{1}{2d} \sum_{n=0}^{N-1} |v_n| \left| \frac{2d - \delta_n \lambda \cos \vartheta}{2d^{(n)}} \right| \\ &\leq \frac{1}{2d} \sum_{n=0}^{N-1} \left| \frac{2d - \delta_n \lambda \cos \vartheta}{2d^{(n)}} \right|. \end{aligned} \quad (34)$$

To further simplify (34), we first analyze the squared distance $(d^{(n)})^2$ by completing the square.

$$\begin{aligned} &(d^{(n)})^2 \\ &= d^2 + \frac{\delta_n^2 \lambda^2}{4} - d\delta_n \lambda \cos \vartheta \\ &= \left(d^2 - d\delta_n \lambda \cos \vartheta + \frac{\delta_n^2 \lambda^2}{4} \cos^2 \vartheta \right) + \frac{\delta_n^2 \lambda^2}{4} - \frac{\delta_n^2 \lambda^2}{4} \cos^2 \vartheta \\ &= \left(d - \frac{\delta_n \lambda}{2} \cos \vartheta \right)^2 + \frac{\delta_n^2 \lambda^2}{4} (1 - \cos^2 \vartheta) \\ &= \left(d - \frac{\delta_n \lambda}{2} \cos \vartheta \right)^2 + \left(\frac{\delta_n \lambda}{2} \sin \vartheta \right)^2. \end{aligned} \quad (35)$$

Now, we substitute (35) into (34):

$$\begin{aligned} \left| \frac{2d - \delta_n \lambda \cos \vartheta}{2d^{(n)}} \right| &= \left| \frac{2(d - \frac{\delta_n \lambda}{2} \cos \vartheta)}{2\sqrt{(d - \frac{\delta_n \lambda}{2} \cos \vartheta)^2 + (\frac{\delta_n \lambda}{2} \sin \vartheta)^2}} \right| \\ &= \frac{|d - \frac{\delta_n \lambda}{2} \cos \vartheta|}{\sqrt{(d - \frac{\delta_n \lambda}{2} \cos \vartheta)^2 + (\frac{\delta_n \lambda}{2} \sin \vartheta)^2}}. \end{aligned}$$

To simplify, let $X = d - \frac{\delta_n \lambda}{2} \cos \vartheta$ and $Y = \frac{\delta_n \lambda}{2} \sin \vartheta$. The expression becomes $\frac{|X|}{\sqrt{X^2 + Y^2}}$.

Since $Y^2 \geq 0$, the denominator $\sqrt{X^2 + Y^2}$ is always greater than or equal to $\sqrt{X^2} = |X|$. This leads to the following strict inequality:

$$\frac{|X|}{\sqrt{X^2 + Y^2}} \leq 1. \quad (36)$$

This demonstrates that $\left| \frac{2d - \delta_n \lambda \cos \vartheta}{2d^{(n)}} \right| \leq 1$ for all n , d , and ϑ .

Finally, we have

$$\frac{1}{2d} \sum_{n=0}^{N-1} \left| \frac{2d - \delta_n \lambda \cos \vartheta}{2d^{(n)}} \right| \leq \frac{1}{2d} \sum_{n=0}^{N-1} (1) = \frac{N}{2d}. \quad (37)$$

Consequently, we conclude that the range derivative satisfies:

$$\left| \frac{\partial S}{\partial d} \right| \leq \left(\frac{\lambda}{4\pi d^2} + \frac{1}{2d} \right) N \quad (38)$$

The derivative of the magnitude satisfies

$$\frac{\partial |S|}{\partial x} = \left| \frac{\partial S}{\partial x} \right| \cos \phi_x, \quad x \in \{d, \vartheta\}, \quad (39)$$

where $\cos \phi_x$ is a phase-alignment factor with $|\cos \phi_x| \leq 1$ and is independent of the array size N . Thus, the scalings in N of $|\partial |S| / \partial x|$ and $|\partial S / \partial x|$ are identical. Thus, we have

$$\frac{\partial |S|}{\partial \vartheta} \leq \cos(\phi_\vartheta) \frac{5\lambda |\sin \vartheta|}{16d_{\min}} N^2 \quad (40)$$

$$\frac{\partial |S|}{\partial d} \leq \cos(\phi_d) \left(\frac{\lambda}{4\pi d^2} + \frac{1}{2d} \right) N. \quad (41)$$

APPENDIX B PROOF OF THEOREM 2

Consider the function $f(d) = (1+d)^\beta$. Its ℓ th derivative is given by

$$f^{(\ell)}(d) = \beta(\beta-1) \cdots (\beta-\ell+1)(1+d)^{\beta-\ell},$$

which can be rewritten as

$$f^{(\ell)}(d) = \ell! \prod_{j=0}^{\ell-1} \frac{\beta-j}{j+1} \cdot (1+d)^{\beta-\ell}. \quad (42)$$

We now bound each term in the product in (42). For each index $0 \leq j \leq \ell-1$, we have

$$\left| \frac{\beta-j}{j+1} \right| = \left| 1 - \frac{\beta+1}{j+1} \right| \leq 1 + \frac{|\beta+1|}{j+1} \leq 1 + |\beta+1|.$$

Denote $M_0 = 1 + |\beta+1|$. Since there are ℓ factors in the product, the over all bound becomes

$$\left| \ell! \prod_{j=0}^{\ell-1} \frac{\beta-j}{j+1} \right| \leq \ell! M_0^\ell.$$

From (42), we thus have

$$\left| f^{(\ell)}(d) \right| \leq \ell! M_0^\ell (1+d)^{\beta-\ell}. \quad (43)$$

Since $1+d$ is bounded, as $d \in \mathcal{D}$, it is clearly that $|(1+d)^{\beta-\ell}| \leq M_1$, thus, combining this with (43) gives

$$\left| f^{(\ell)}(d) \right| \leq \ell! M_1 M_0^\ell \leq \ell! C_1^\ell,$$

where $C_1 = M_1^{1/\ell} M_0$.

This derivative growth condition satisfies the hypothesis of Theorem 11.22 in [39], which guarantees that, for sufficiently small fill distance h , the interpolation error decays exponentially

$$\|f - \rho\|_{L_\infty(\mathcal{D})} \leq e^{-c/h} |f|_{\mathcal{N}_\phi(\mathcal{D})}.$$

This completes the proof of Theorem 2.

REFERENCES

- [1] J. Chen and U. Mitra, "Unimodality-constrained matrix factorization for non-parametric source localization," *IEEE Trans. Signal Process.*, vol. 67, no. 9, pp. 2371–2386, Mar. 2019.
- [2] Y. Zeng, J. Chen, J. Xu, D. Wu, X. Xu, S. Jin, X. Gao, D. Gesbert, S. Cui, and R. Zhang, "A tutorial on environment-aware communications via channel knowledge map for 6g," *IEEE Commun. Surv. Tutor.*, vol. 26, no. 3, pp. 1478–1519, Feb. 2024.
- [3] X. Yu, J. Zhang, M. Haenggi, and K. B. Letaief, "Coverage analysis for millimeter wave networks: The impact of directional antenna arrays," *IEEE J. Sel. Areas Commun.*, vol. 35, no. 7, pp. 1498–1512, Apr. 2017.
- [4] H. Lei, J. Zhang, Z. Wang, B. Ai, and E. Björnson, "Near-field user localization and channel estimation for XL-MIMO systems: Fundamentals, recent advances, and outlooks," *IEEE Wirel. Commun.*, vol. 32, no. 4, pp. 190–198, Aug. 2025.
- [5] M. Cui, Z. Wu, Y. Lu, X. Wei, and L. Dai, "Near-field MIMO communications for 6G: Fundamentals, challenges, potentials, and future directions," *IEEE Commun. Mag.*, vol. 61, no. 1, pp. 40–46, Sep. 2023.
- [6] K. Sato and T. Fujii, "Kriging-based interference power constraint: Integrated design of the radio environment map and transmission power," *IEEE Trans. Cogn. Commun. Netw.*, vol. 3, no. 1, pp. 13–25, Jan. 2017.
- [7] K. Sato, K. Suto, K. Inage, K. Adachi, and T. Fujii, "Space-frequency-interpolated radio map," *IEEE Trans. Veh. Technol.*, vol. 70, no. 1, pp. 714–725, Jan. 2021.
- [8] Y. Teganya, D. Romero, L. M. L. Ramos, and B. Beferull-Lozano, "Location-free spectrum cartography," *IEEE Trans. Signal Process.*, vol. 67, no. 15, pp. 4013–4026, Jun. 2019.
- [9] J. A. Bazerque and G. B. Giannakis, "Nonparametric basis pursuit via sparse kernel-based learning: A unifying view with advances in blind methods," *IEEE Signal Process. Mag.*, vol. 30, no. 4, pp. 112–125, Jul. 2013.
- [10] Y.-Q. Xu, B. Zhang, X. Zhang, J. Hu, and D. Guo, "Radio environment map construction with Gaussian process and kernel transformation," in *Proc. IEEE Int. Conf. Commun., Image and Signal Processing*, Chengdu, China, Nov. 2021, pp. 350–355.
- [11] M. Hamid and B. Beferull-Lozano, "Non-parametric spectrum cartography using adaptive radial basis functions," in *Proc. IEEE Int. Conf. Acoustics, Speech, Signal Processing*, 2017, pp. 3599–3603.
- [12] Z. Xu, B. Huang, and B. Jia, "An efficient radio map learning scheme based on kernel density function," *IEEE Trans. Veh. Technol.*, vol. 70, no. 12, pp. 13 315–13 324, Oct. 2021.
- [13] J. Wang, Q. Zhu, Z. Lin, Q. Wu, Y. Huang, X. Cai, W. Zhong, and Y. Zhao, "Sparse bayesian learning-based 3D radio environment map construction-sampling optimization, scenario-dependent dictionary construction, and sparse recovery," *IEEE Trans. Cogn. Commun. Netw.*, vol. 10, no. 1, pp. 80–93, Oct. 2024.
- [14] J. Wang, Q. Zhu, Z. Lin, J. Chen, G. Ding, Q. Wu, G. Gu, and Q. Gao, "Sparse bayesian learning-based hierarchical construction for 3D radio environment maps incorporating channel shadowing," *IEEE Trans. Wireless Commun.*, vol. 23, no. 10, pp. 14 560–14 574, Oct. 2024.
- [15] Q. Gao, Q. Zhu, Z. Lin, P. T. Mathiopoulos, Y. Zhao, Y. Huang, J. Wang, and Q. Wu, "Time-variant radio map reconstruction with optimized distributed sensors in dynamic spectrum environments," *IEEE Internet Things J.*, vol. 12, no. 12, pp. 20 927–20 941, Feb. 2025.
- [16] S.-J. Kim and G. B. Giannakis, "Cognitive radio spectrum prediction using dictionary learning," in *Proc. IEEE Global Telecomm. Conf.*, Atlanta, GA, USA, Jun. 2013, pp. 3206–3211.
- [17] M. D. Migliore, "A compressed sensing approach for array diagnosis from a small set of near-field measurements," *IEEE Trans. Antennas Propag.*, vol. 59, no. 6, pp. 2127–2133, Apr. 2011.
- [18] H. Sun and J. Chen, "Grid optimization for matrix-based source localization under inhomogeneous sensor topology," in *Proc. IEEE Int. Conf. Acoustics, Speech, Signal Processing*, Toronto, ON, Canada, Jun. 2021, pp. 5110–5114.
- [19] H. Xia, S. Zha, J. Huang, J. Liu, and P. Liu, "Spectrum cartography based on dynamic compressed sensing by using multiple domains information," *J. Commun. Net.*, vol. 25, no. 4, pp. 507–515, Aug. 2023.
- [20] T.-H. Chou, N. Michelusi, D. J. Love, and J. V. Krogmeier, "Fast position-aided mimo beam training via noisy tensor completion," *IEEE J. Sel. Top. Signal Process.*, vol. 15, no. 3, pp. 774–788, Mar. 2021.
- [21] D. Schaufele, R. L. G. Cavalcante, and S. Stanczak, "Tensor completion for radio map reconstruction using low rank and smoothness," in *Proc. IEEE Int. Workshop Signal Process. Adv. Wireless Commun.*, Cannes, France, Jul. 2019, pp. 1–5.
- [22] L. Ma, W. Zhao, Y. Xu, and C. Li, "Radio map efficient building method using tensor completion for WLAN indoor positioning system," in *Proc. IEEE Int. Conf. Commun.*, Kansas City, MO, USA, May 2018, pp. 1–6.
- [23] F. Shen, Z. Wang, G. Ding, K. Li, and Q. Wu, "3D compressed spectrum mapping with sampling locations optimization in spectrum-heterogeneous environment," *IEEE Trans. Wireless Commun.*, vol. 21, no. 1, pp. 326–338, Jul. 2022.
- [24] H. Sun and J. Chen, "Integrated interpolation and block-term tensor decomposition for spectrum map construction," *IEEE Trans. Signal Process.*, vol. 72, pp. 3896–3911, Aug. 2024.
- [25] X. Chen, J. Wang, and Q. Huang, "Dynamic spectrum cartography: Reconstructing spatial-spectral-temporal radio frequency map via tensor completion," *IEEE Trans. Signal Process.*, vol. 73, pp. 1184–1199, Jan. 2025.
- [26] H. Sun, J. Chen, and Y. Luo, "Tensor-guided interpolation for off-grid power spectrum map construction," in *Proc. IEEE Int. Conf. Acoustics, Speech, Signal Processing*, Seoul, Korea, Apr. 2024, pp. 7295–7299.
- [27] L. Xu, L. Cheng, J. Chen, W. Pu, and X. Fu, "Radio map estimation via latent-domain plug-and-play denoisers," in *Proc. IEEE Int. Conf. Acoustics, Speech, Signal Process.*, Hyderabad, India, Apr. 2025, pp. 1–5.
- [28] S. Timilsina, S. Shrestha, and X. Fu, "Quantized radio map estimation using tensor and deep generative models," *IEEE Trans. Signal Process.*, vol. 72, pp. 173–189, Nov. 2024.
- [29] W. Chen and J. Chen, "Diffraction and scattering aware radio map and environment reconstruction using geometry model-assisted deep learning," *IEEE Trans. Wireless Commun.*, vol. 23, no. 12, pp. 19 804–19 819, Nov. 2024.
- [30] S. Shrestha, X. Fu, and M. Hong, "Deep spectrum cartography: Completing radio map tensors using learned neural models," *IEEE Trans. Signal Process.*, vol. 70, pp. 1170–1184, Jan. 2022.
- [31] X. Luo, Z. Li, Z. Peng, M. Chen, and Y. Liu, "Denoising diffusion probabilistic model for radio map estimation in generative wireless networks," *IEEE Trans. Cognitive Commun. Networking*, vol. 11, no. 2, pp. 751–763, Jan. 2025.
- [32] H. Sun and J. Chen, "Propagation map reconstruction via interpolation assisted matrix completion," *IEEE Trans. Signal Process.*, vol. 70, pp. 6154–6169, Dec. 2022.
- [33] Y. Zhang and S. Wang, "K-nearest neighbors Gaussian process regression for urban radio map reconstruction," *IEEE Commun. Lett.*, vol. 26, no. 12, pp. 3049–3053, Sep. 2022.
- [34] X. Chen, J. Wang, G. Zhang, and Q. Peng, "Tensor-based parametric spectrum cartography from irregular off-grid samplings," *IEEE Signal Process. Lett.*, vol. 30, pp. 513–517, Mar. 2023.
- [35] H. Sun and J. Chen, "Energy-modified leverage sampling for radio map construction via matrix completion," *IEEE Signal Process. Lett.*, vol. 31, pp. 1780–1784, Jun. 2024.
- [36] H. Dong, W. Pu, R. Zhou, X. Fu, and F. Yin, "Integrated interpolation and matrix completion for radio map estimation: A convex optimization approach," in *Proc. IEEE Int. Conf. Acoustics, Speech, Signal Processing*, Hyderabad, India, Apr. 2025, pp. 1–5.
- [37] H. Sun and J. Chen, "Regression assisted matrix completion for reconstructing a propagation field with application to source localization," in *Proc. IEEE Int. Conf. Acoustics, Speech, Signal Processing*, Singapore, May 2022, pp. 3353–3357.
- [38] M. R. Akdeniz, Y. Liu, M. K. Samimi, S. Sun, S. Rangan, T. S. Rappaport, and E. Erkip, "Millimeter wave channel modeling and cellular capacity evaluation," *IEEE J. Sel. Areas Commun.*, vol. 32, no. 6, pp. 1164–1179, Jun. 2014.
- [39] H. Wendland, *Scattered data approximation*. Cambridge university press, 2004, vol. 17.
- [40] F. A. Potra and S. J. Wright, "Interior-point methods," *Journal of computational and applied mathematics*, vol. 124, no. 1-2, pp. 281–302, Dec. 2000.
- [41] P. Jain and P. Netrapalli, "Fast exact matrix completion with finite samples," in *Conference on Learning Theory*. PMLR, Jun. 2015, pp. 1007–1034.
- [42] E. J. Candes and Y. Plan, "Matrix completion with noise," *Proceedings of the IEEE*, vol. 98, no. 6, pp. 925–936, Apr. 2010.
- [43] J. Fan, *Local polynomial modelling and its applications: Monographs on statistics and applied probability 66*. Routledge, 1996.
- [44] A. Verdin, C. Funk, B. Rajagopalan, and W. Kleiber, "Kriging and local polynomial methods for blending satellite-derived and gauge precipitation estimates to support hydrologic early warning systems," *IEEE Trans. Geosci. Remote Sens.*, vol. 54, no. 5, pp. 2552–2562, Jan. 2016.